Nano Research

ISSN 1998-0124 CN 11-5974/O4
https://doi.org/10.26599/NR.2026.94909271

Research Article

Multi-component ultra-high-temperature boride ceramic whiskers with enhanced electromagnetic wave absorption

Yixin Li[1], Yanqin Fu[2](✉), Junhao Zhao[1], Jian Zhang[1], Qingzhe Cui[1], Jiachen Li[1], Junshuai Lv[1], Liyuan Han[2], Ruiyi Su[3], Tien Zhang[3], Yulei Zhang[1,2](✉), Hejun Li[1]

[1] Shaanxi Key Laboratory of Fiber Reinforced Light Composite Materials, Science and Technology on Thermostructural Composite Materials Laboratory, Northwestern Polytechnical University, Xi'an 710072, China

[2] Henan Key Laboratory of High Performance Carbon Fiber Reinforced Composites, Institute of Carbon Matrix Composites, Henan Academy of Sciences, Zhengzhou 450046, China

[3] General Design Department of Beijing Mechanical and Electrical Engineering, Beijing 100089, China

Nano Res., **Just Accepted Manuscript** • https://doi.org/10.26599/NR.2026.94909271

https://www.sciopen.com/journal/1998-0124 on Oct. 19, 2026

© The Authors(s)

Just Accepted

This is a "Just Accepted" manuscript, which has been examined by the peer-review process and has been accepted for publication. A "Just Accepted" manuscript is published online shortly after its acceptance,which is prior to technical editing and formatting and author proofing. Tsinghua University Press (TUP) provides "Just Accepted" as an optional and free service which allows authors to make their results available to the research community as soon as possible after acceptance. After a manuscript has been technically edited and formatted, and the page proofs have been corrected, it will be removed from the "Just Accepted" web site and published officially with volume and article number (e.g., *Nano Research*, **2025**, *18*, 94906990). Please note that technical editing may introduce minor changes to the manuscript text and/or graphics which may affect the content, and all legal disclaimers that apply to the journal pertain. In no event shall TUP be held responsible for errors or consequences arising from the use of any information contained in these "Just Accepted" manuscripts. To cite this anuscript please use its Digital Object Identifier (DOI®),which is identical for all formats of publication.

Just Accepted

Research Article

Multi-component ultra-high-temperature boride ceramic whiskers with enhanced electromagnetic wave absorption

Yixin Li[1], Yanqin Fu[2]*, Junhao Zhao[1], Jian Zhang[1], Qingzhe Cui[1], Jiachen Li[1], Junshuai Lv[1], Liyuan Han[2], Ruiyi Su[3], Tien Zhang[3], Yulei Zhang[1,2]*, and Hejun Li[1]

[1] *Shaanxi Key Laboratory of Fiber Reinforced Light Composite Materials, Science and Technology on Thermostructural Composite Materials Laboratory, Northwestern Polytechnical University, Xi'an, 710072, China*

[2] *Henan Key Laboratory of High Performance Carbon Fiber Reinforced Composites, Institute of Carbon Matrix Composites, Henan Academy of Sciences, Zhengzhou 450046, China*

[3] *General Design Department of Beijing Mechanical and Electrical Engineering, Beijing 100089, China*

**Corresponding author.*

Received: 1 August 2026; **Revised:** 30 September 2026; **Accepted:** 19 October 2026

✉Address correspondence to Yanqin Fu, fuyanqin@hnas.ac.cn; Yulei Zhang, zhangyulei@nwpu.edu.cn

Cite this article: Nano Research, 2026, 19, 94909271 https://doi.org/10.26599/NR.2026.94909271

Just Accepted

Abstract

Boride ceramics have emerged as promising candidates for electromagnetic wave (EMW) absorption due to their thermal stability and conductivity. However, their intrinsically high conductivity often causes impedance mismatch with free space. Herein, multi-component boride whiskers were prepared. Benefiting from compositional design, the $(Hf_{2/5}Zr_{2/5}Ti_{1/5})B_2$ whiskers

exhibit effective EMW absorption performance at room temperature, achieving a minimum reflection loss of -60.88 dB at a matching thickness of 2.55 mm. This results from regulating the Ti content, which introduces lattice distortion and charge inhomogeneities, establishing abundant relaxation-type dipole centers to enhance polarization loss. Simultaneously, the interconnected whisker network facilitates carrier transport, boosting conductive loss. Crucially, after heat treatment at 1500 °C, the whiskers preserve structural integrity, and the $(Hf_{1/3}Zr_{1/3}Ti_{1/3})B_2$ exhibits improved performance, achieving an ultra-wide effective absorption bandwidth of 8.64 GHz at a thickness of only 2.50 mm. This improvement stems from promoted electron transport and optimized impedance matching. This work provides a strategy for developing ultra-wideband and thermally stable EMW absorbers in extreme environments.

Keywords: $(Hf,Zr,Ti)B_2$ whiskers, multi-component boride, solid solution, electromagnetic wave absorption

1. Introduction

With the increasing Mach number of stealth aircraft, higher requirements have been put forward for the radar stealth systems of hot-end components, which are subjected to complex electromagnetic detection scenarios and extreme aerodynamic heating environments [1–3]. However, traditional electromagnetic wave (EMW) absorbing materials suffer from inherent drawbacks; for instance, ferrites undergo demagnetization and lose their magnetic loss capability once the temperature reaches the Curie temperature, while polymer-based absorbers exhibit insufficient thermal stability [4–6]. Hence, developing high-performance EMW absorbers with both thermal stability and environmental stability remains a critical challenge for their practical engineering applications.

Ultra-high-temperature ceramics (UHTCs), including transition metal carbides [7–11], borides

Just Accepted

[12–15] and nitrides [16,17], exhibit ultra-high melting points (>3000 °C) [18] and excellent oxidation resistance. Among them, transition metal borides possess relatively high conductive loss due to their unique AlB_2-type hexagonal crystal structure and bonding mode, thus serving as ideal candidates for EMW absorption in harsh high-temperature environments [19]. However, due to the pronounced impedance mismatch caused by their inherent high electrical conductivity [20], single-component boride ceramics like ZrB_2 or HfB_2 [21–23] typically reflect most EMW at the surface, yielding an insufficient minimum reflection loss (RL_{min}) and a narrow effective absorption bandwidth (EAB). In recent years, the concept of multi-principal component ceramics has offered an effective approach to resolving these issues. By introducing multiple metallic cations into a single lattice, a single-phase solid solution is formed with an entropy-stabilization effect [24–27], which usually possesses lattice distortion, local charge inhomogeneities, and vacancies [28,29]. For instance, Zhu et al. [30] synthesized a series of high-entropy carbide nanowires with varying configurational entropy and systematically evaluated their EMW absorption performance. They demonstrated that such structural distortions can change the electron transport, thereby successfully balancing the dielectric constant and optimizing impedance matching. Meanwhile, these lattice defects act as prominent polarization centers under alternating electric fields, enhancing dielectric loss. In addition, Zhang et al. [31] synthesized three types of high-entropy transition metal diborides, among which the $(Cr_{0.2}Zr_{0.2}Hf_{0.2}Nb_{0.2}Ta_{0.2})B_2$ ceramic achieved a RL_{min} of −56.2 dB alongside an EAB_{max} of 11.0 GHz. Their results indicated that regulating the composition of CrB_2 could significantly optimize the impedance matching, yielding highly efficient and broadband absorption characteristics. However, the role of solid-solution-induced lattice distortion and local charge inhomogeneity in regulating relaxation polarization, dielectric loss, and impedance matching has not

Just Accepted

yet been clarified.

Apart from composition design, microstructure design has also been proven to effectively improve dielectric loss and EMW performance, a strategy that reduces the dependence on additional heterogeneous interfaces and structural complexity. For example, Hu et al. [32] synthesized $(Zr_{5/12}Hf_{5/12}Ta_{1/12}Ti_{1/12})B_2$ and $(Zr_{5/12}Hf_{5/12}Ta_{1/12}Cr_{1/12})B_2$ samples with hollow spherical structures, achieving RL_{min} values of -53.56 dB and -68.07 dB, along with an EAB of 4.88 GHz and 3.20 GHz, respectively. Additionally, ceramic whiskers are also widely recognized as a highly promising structure for EMW absorption. For instance, rod-like ZrB_2 obtained by Liu et al. [33] through precursor pyrolysis at 1500 °C achieved a RL_{min} of -54.77 dB at a thickness of 4.7 mm. The results suggested that rod-like network structures induced robust conduction loss and multiple scattering, enhancing the EMW dissipation efficiency.

In this work, we demonstrate a multi-component whisker design strategy that integrates conductive and polarization losses. Three types of multi-component boride whiskers, namely $(Hf_{9/20}Zr_{9/20}Ti_{1/10})B_2$, $(Hf_{2/5}Zr_{2/5}Ti_{1/5})B_2$, and $(Hf_{1/3}Zr_{1/3}Ti_{1/3})B_2$, with uniform diameters and single-crystalline hexagonal structures, were synthesized via a molten salt-assisted boro-carbothermal reduction method. The Ti content is systematically tuned to tailor lattice distortion and local charge inhomogeneity, realizing the synergistic optimization of dielectric polarization loss and impedance matching. The whiskers provide continuous pathways for carrier transport and contribute to conductive loss and multiple EMW scattering. Furthermore, the EMW absorption performance and attenuation mechanism after 1500 °C heat treatment are further investigated, thereby alleviating electron-transport barriers between whiskers and strengthening the interfacial coupling.

Just Accepted

2. Experimental

2.1 Experimental procedure

Commercially available HfO_2, ZrO_2, and TiO_2 powders (>99.9%, 1-3 μm), B_4C powder (>99.9%, ~2.5 μm, both from Qinhuangdao Eno Material Development Co. Ltd, China), and NaCl/KCl (99.5% purity; Tianjin Damao Chemical Reagent Factory) were mixed according to the calculated stoichiometric ratio. The composition ratio was as follows: (HfO_2, ZrO_2, TiO_2, B_4C): (NaCl, KCl) = 1:1 (mass ratio), where NaCl: KCl = 1:1 (molar ratio). Different samples were designed with the Hf and Zr contents fixed at a 1:1 molar ratio, and Ti content varied. $(Hf_{9/20}Zr_{9/20}Ti_{1/10})B_2$, $(Hf_{2/5}Zr_{2/5}Ti_{1/5})B_2$, and $(Hf_{1/3}Zr_{1/3}Ti_{1/3})B_2$ whiskers were fabricated, which were denoted as HZTB-1, HZTB-2, and HZTB-3, respectively.

Firstly, the above reaction raw materials were homogenized for 6 h using a planetary ball mill (Y_2O_3-stabilized ZrO_2 balls were used as the grinding media). After ball milling, the ZrO_2 balls were separated by sieving through a 50-mesh sieve. Subsequently, the obtained mixed powders were loaded into a crucible lined with graphite paper, and the crucible was then placed in a horizontal alumina tube furnace. The furnace was heated to the target temperature at a rate of 8 °C /min, held for 2 h, and then cooled to room temperature at a rate of 3 °C /min. The whole process was under a flowing argon atmosphere. The synthesized product was collected, washed with 50 °C deionized water to remove residual NaCl/KCl salts, and dried in an oven to obtain the final product. For EMW absorption testing, the as-prepared samples were mixed with paraffin at a mass ratio of 30 wt%, and the mixture was then pressed into hollow annular specimens with an inner diameter of 3.04 mm and an outer diameter of 7.00 mm. Specifically, the as-prepared whisker powders were heat-treated at 1500 °C for 2 h, and remixed with paraffin at the same mass fraction of 30 wt% after cooling to

Just Accepted

room temperature, then repressed into coaxial ring specimens for subsequent electromagnetic testing. The schematic diagram of the preparation process is illustrated in Fig. 1.

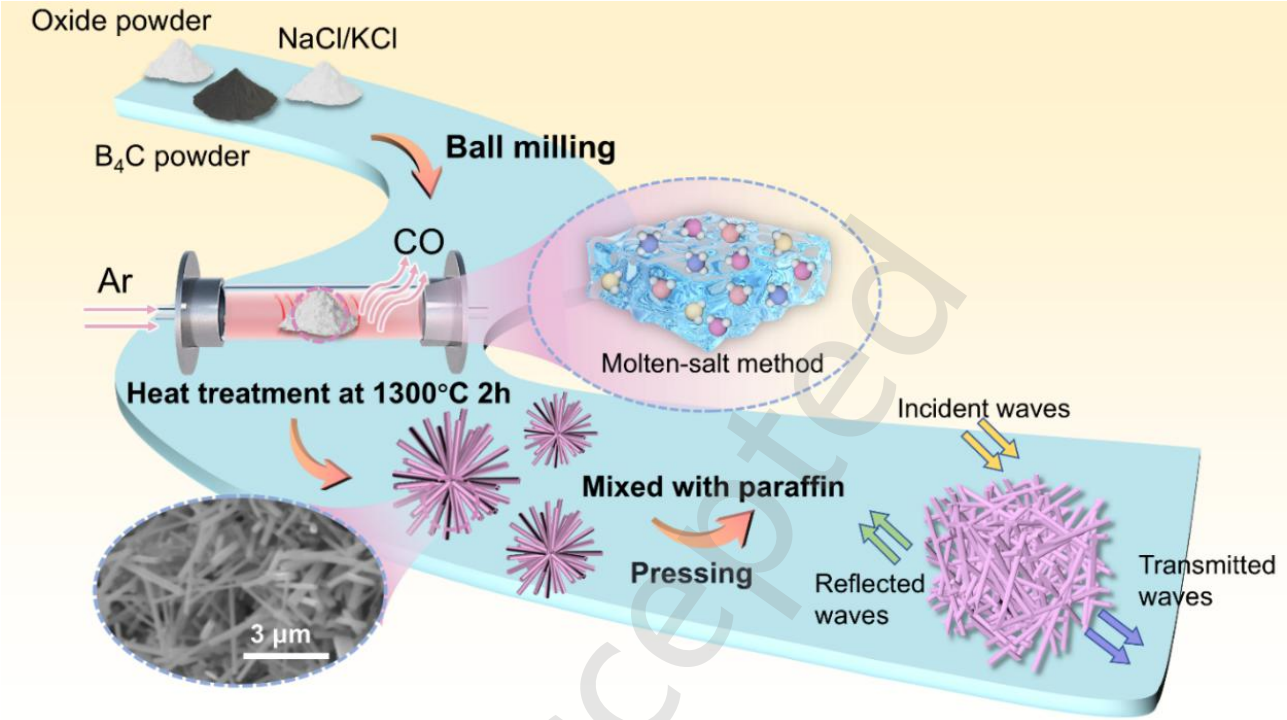


Fig. 1. Schematic diagram of the whisker synthesis process and EMW-absorbing test.

2.2 **Characterization**

The phase composition of the as-prepared samples was characterized by X-ray diffractometry (XRD, X'Pert PRO; PANalytical, Almelo), and the XRD patterns were collected with a step size of 0.02 ° and a scanning speed of 2 ° min^{-1}. The microstructure, elemental distribution, and fine structural information of the products were characterized by scanning electron microscopy (SEM, JSM6460; ZEISS EVO10) equipped with an energy-dispersive spectrometer (EDS, JSM-6460), while the nanostructure and detailed compositional information were further analyzed via transmission electron microscopy (TEM, Talos F200X, FEI, USA) coupled with an EDS detector (INCA, Oxford Instruments, UK). The thermal behavior of the precursor during the reaction process was investigated using a thermogravimetric analyzer (TGA, NETZSCH STA 449F5). For

Just Accepted

electromagnetic performance evaluation, the complex permittivity of the samples in the 2-18 GHz frequency range was measured with a vector network analyzer (N5225B, KEYSIGHT) via the coaxial line method, and the corresponding far-field radar cross section (RCS) values were simulated using CST Studio Suite 2025. The simulation model used a 200 mm square composed of an upper absorbing layer (HZTB-1, 1.95 mm; HZTB-2, 2.55 mm) and a bottom perfect electric conductor layer (PEC, 1 mm). The model plate was placed on the XOY plane.

3. Results and discussion

3.1 Fabrication and microstructure of whiskers

The feasibility of forming single-phase solid solution was evaluated by calculating the lattice size difference, followed by thermodynamic calculations using HSC 6.0 software (Eq. S(1)-S(9)). These results indicated that the preparation of the three boride ceramics was theoretically feasible, as the Gibbs free energy change (ΔG) of the reaction became negative before 1300 °C (Fig. S1), which agreed with the XRD patterns (Fig. S2) that HZTB-1, HZTB-2, and HZTB-3 were successfully synthesized at 1300 °C. As displayed in the XRD patterns (Fig. 2(a)), all as-prepared samples exhibit the characteristic diffraction peaks of diborides with no detectable oxide diffraction peaks. Notably, the diffraction peaks shifted toward higher angles with increasing Ti content, which can be attributed to the larger cationic radii of Hf and Zr than those of Ti (Hf^{4+}: 0.71 Å, Zr^{4+}: 0.72 Å, Ti^{4+}: 0.61 Å).

In situ TG-DSC was employed to further analyze the reaction process, as shown in Fig. 2(b). The mass loss can be divided into four distinct stages with increasing temperature. From room temperature to 700 °C, no significant mass loss was observed, and an endothermic feature at 652.5 °C corresponded to the melting of the NaCl-KCl eutectic. In the 700-900 °C stage, a notable

Just Accepted

mass loss of 17.9% was observed, accompanied by a DTG peak at 886.7 °C, indicating continuous release of CO gas during boro-carbothermal reduction reaction and the volatilization of molten salt. Upon entering the 900-1100 °C regime, the reaction rate accelerated. An endothermic feature at 932 °C indicated the continued progression of the reduction reaction, while the DTG peak value at 1069.6 °C signified that this interval represents the core reaction stage with the primary mass loss of 29.2%. Correspondingly, the exothermic peak at 1089.1 °C is attributed to the intensive nucleation and crystallization of the boride whiskers, which releases substantial latent heat concurrent with the peak reaction rate. Finally, in the 1100-1300 °C region, a further mass loss of 6.3% resulted from further volatilization of molten salt. The TG curve stabilized above 1300 °C, signifying that the reaction was essentially completed.

The microstructures of the products are shown in Fig. 2(c-e). When the fabrication temperature was 1300 °C, HZTB-1 and HZTB-2 predominantly exhibited a whisker-like morphology. In contrast, HZTB-3 exhibited a mixed morphology of whiskers and slight portion of particles. Quantitative statistical analysis (Fig. S3) shows that the whisker diameter ranges from 190 to 250 nm, while the whisker length decreases from 2.45 to 1.53 μm with increasing Ti content. Fig. 2(f) shows the EDS elemental maps of the region shown in Fig. 2(c), confirming the uniform distribution of Hf, Zr, and Ti at the microscale. When the synthesis temperature was increased to 1400 °C (Fig. S4), the whiskers experienced substantial coarsening, where adjacent whiskers grew to form larger rod-like crystals or agglomerates, or even transformed into irregular shapes. This indicated that excessively high temperatures are detrimental to the growth of one-dimensional structures. Rietveld refinement of the HZTB-1 sample synthesized at 1300 °C (Fig. 2(g)) yielded R_{wp} = 9.84%, R_p = 6.81%, and χ^2 = 1.080, indicating that the as-prepared product possesses a well-defined hexagonal AlB_2-type crystal

Just Accepted

structure (space group: P6/mmm).

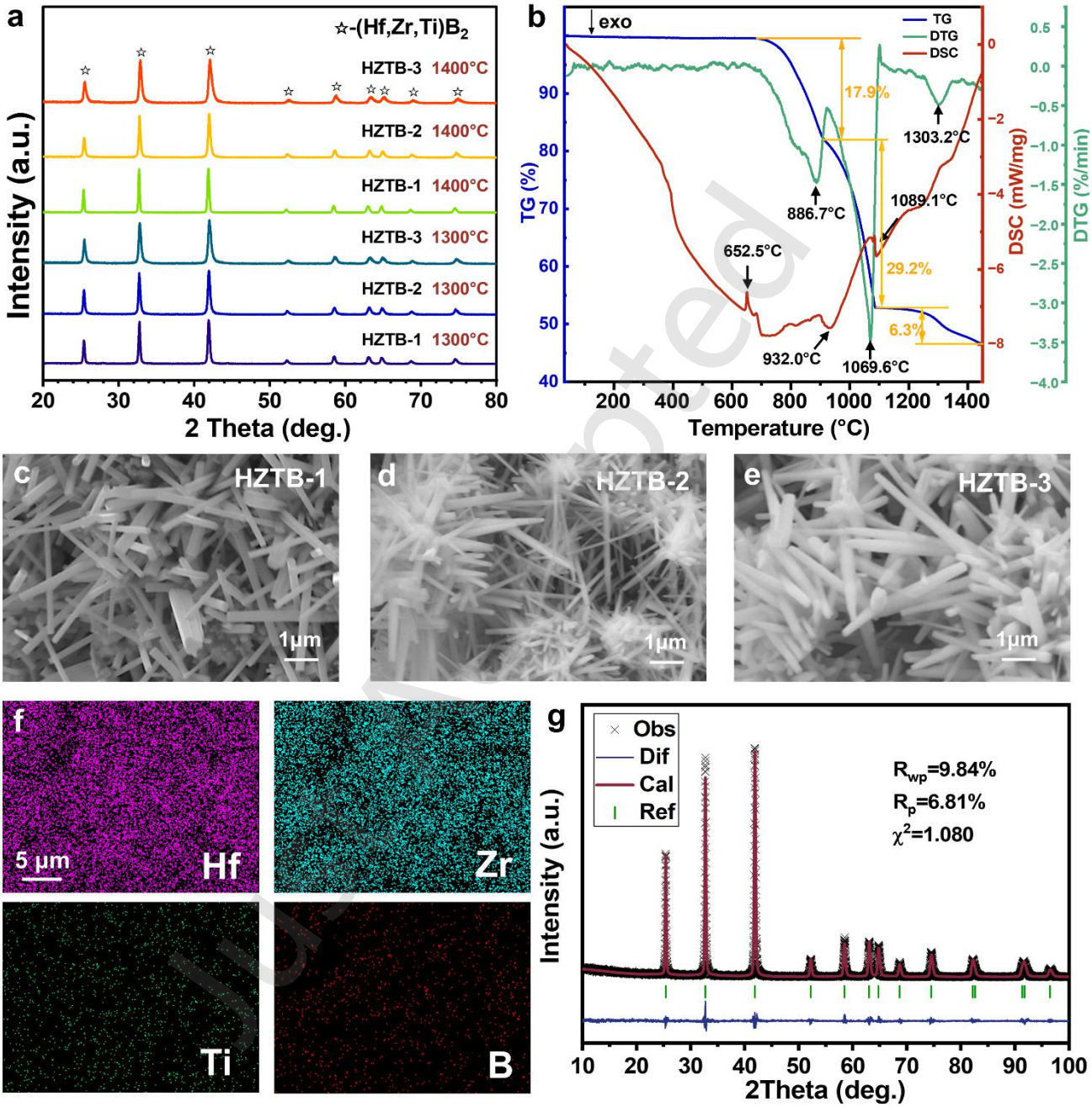


Fig. 2. Phase and microstructure characterizations of the as-prepared whiskers: (a) XRD patterns; (b) TG-DSC curves during the reaction process; (c-e) SEM images of products prepared at 1300 °C; (f) EDS spectrum of the product in (c); (g) XRD pattern refinement of HZTB-1.

The elemental composition of whiskers was investigated via XPS (Fig. S5), and the chemical bonding states of HZTB-1 were analyzed by high-resolution XPS spectra, as shown in Fig. 3. In the

Just Accepted

high-resolution B 1s spectrum (Fig. 3(a)), the peak at 187.49 eV is assigned to B in metal-boride (M-B, M = Hf, Zr, Ti) bonding [34–36], while the peak at 192.2 eV matches well with the B-O bonds [36]. In the Hf 4f spectrum (Fig. 3(b)), two distinct peaks appear at 13.9 eV (Hf $4f_{7/2}$) and 15.5 eV (Hf $4f_{5/2}$) [36] with a spin-orbit splitting value of 1.6 eV, which are attributed to Hf-B bonds. Regarding the Zr 3d spectrum (Fig. 3(c)), the peaks at 178.2 eV (Zr $3d_{5/2}$) and 180.6 eV (Zr $3d_{3/2}$) are ascribed to Zr-B bonds (with a spin-orbit splitting of 2.4 eV) [34,37]. In Fig. 3(d), the Ti 2p spectrum also exhibits two spin-orbit doublets. The peaks at 454.1 eV and 459.8 eV are assigned to Ti $2p_{3/2}$ and Ti $2p_{1/2}$ in Ti-B bonds [35].

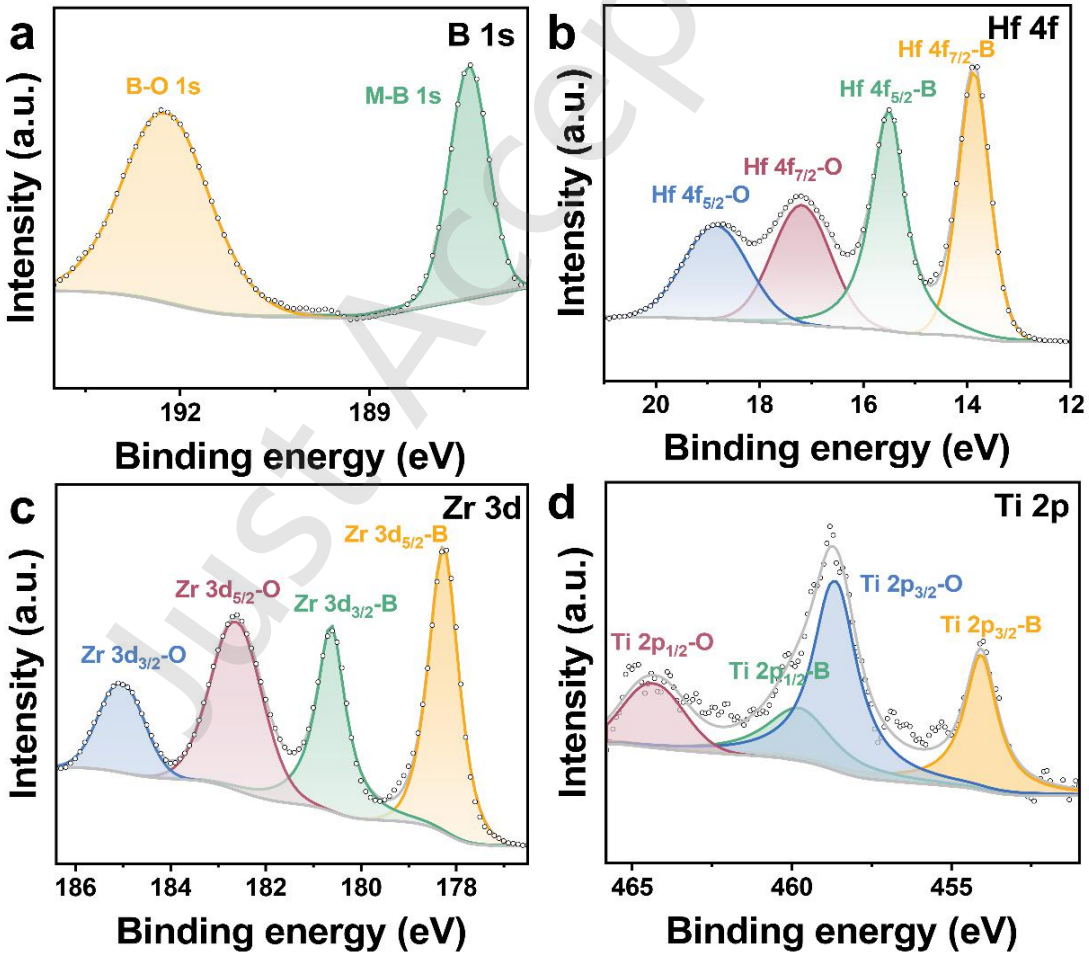


Fig. 3. Peak-fitted high-resolution XPS spectra of the as-prepared HZTB-1 whiskers: (a) B 1s; (b) Hf 4f; (c) Zr 3d; and (d) Ti 2p.

TEM images in Fig. 4 show that the whiskers of HZTB-1, HZTB-2, and HZTB-3 exhibit a

Just Accepted

morphology characterized by smooth surfaces and uniform diameters. HRTEM observations from the edge regions of the whiskers (Fig. 4(a1-c1)) reveal that all three types of whiskers display periodic lattice structures. The corresponding SAED patterns (Fig. 4(a3-c3)) confirmed that the whiskers possess an AlB_2-type single-crystalline hexagonal structure. An amorphous layer can be observed at the edges of all three types of whiskers. Combined with the aforementioned XPS analysis results (Fig. 3), this amorphous layer can be identified as B_2O_3 [38,39]. Notably, the thickness of this amorphous layer increases with increasing Ti content, measuring 3.03 nm for HZTB-1, 3.15 nm for HZTB-2, and significantly thickening to 5.72 nm for HZTB-3. Furthermore, irregular bending and discontinuity of lattice fringes can be observed in the HRTEM image of the HZTB-2 and HZTB-3 whiskers (Fig. 4(b2), (c2)), indicating the presence of more local lattice strain with higher Ti content. The EDS elemental mapping of the whiskers showed that the Hf, Zr, and Ti elements are homogeneously distributed along the longitudinal axis of the whiskers without obvious segregation. Concurrently, further TEM characterization was performed on the non-whisker particulate regions in HZTB-3 (Fig. S6). HRTEM characterization (Fig. S6(d)) revealed that these particles are encapsulated by an amorphous B_2O_3 layer with a thickness of 20-30 nm, which is thicker than that in the whisker regions and suppresses further growth of particles within this region [40].

Just Accepted

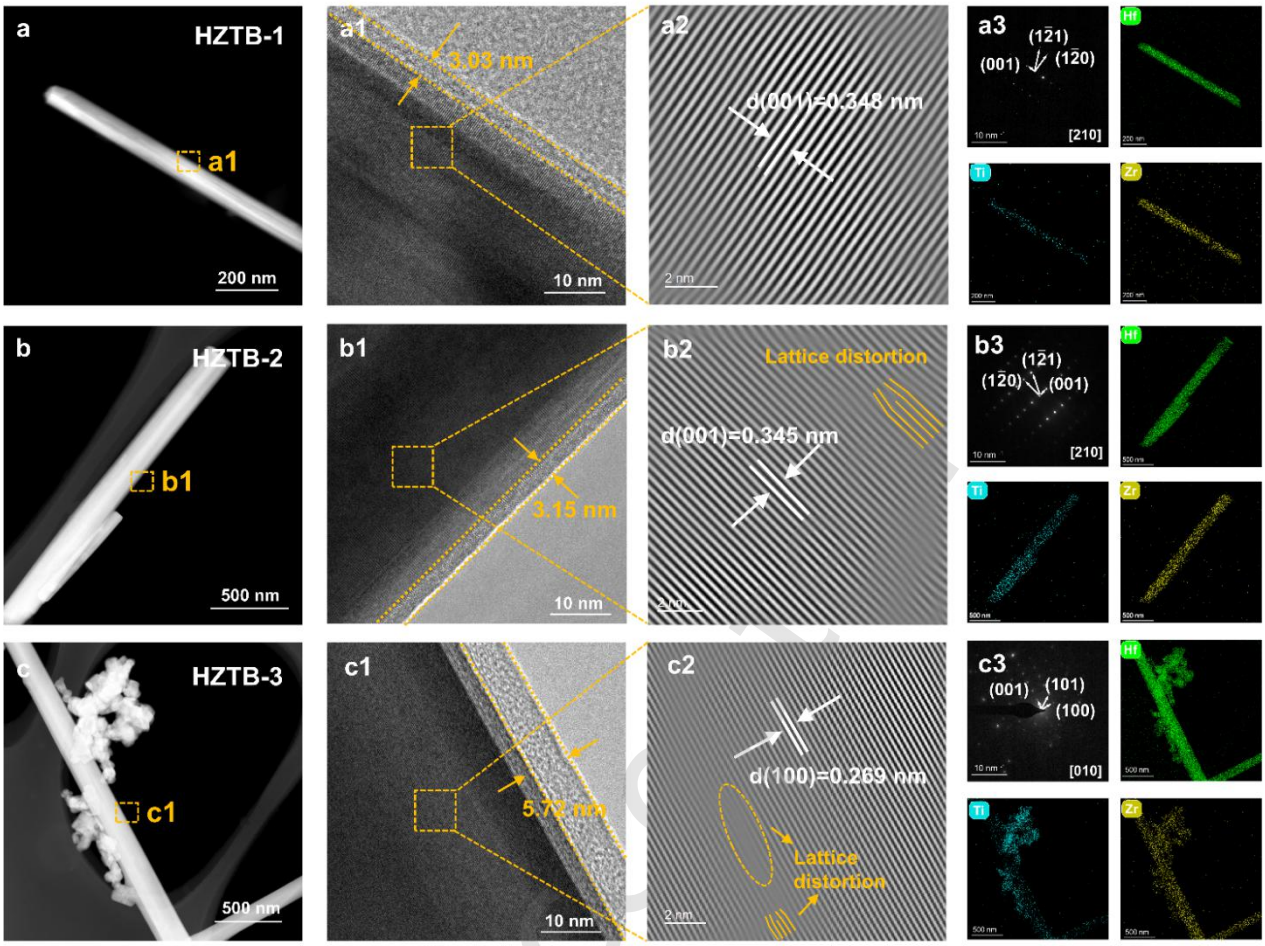


Fig. 4. TEM images and EDS elemental mapping of the whiskers: (a-a3) HZTB-1; (b-b3) HZTB-2; (c-c3) HZTB-3.

3.2 Formation mechanism of whiskers

The formation process of the whiskers can be divided into two stages (Fig. 5(a, c)): the formation of molten salt droplets and the growth of whiskers. Firstly, the NaCl and KCl eutectic melt to form a liquid phase that provides nucleation sites while facilitating the dissociation of metal oxide precursors (HfO_2, ZrO_2, TiO_2) into mobile cations (Hf^{4+}, Zr^{4+}, Ti^{4+}) and O^{2-} ions, while B_4C dissociates into reactive boron species. As the reaction proceeds within these molten droplets, the local concentration of the constituent ions reaches a supersaturated state, leading to the nucleation and precipitation of the (Hf, Zr, Ti)B_2 phase. The second stage involves anisotropic growth into whisker-like morphologies. According to Wulff's construction, differences in surface energy

Just Accepted

determine the relative stability of different crystallographic surfaces and thus the equilibrium crystal morphology. Initially, supersaturation induces the precipitation of (Hf, Zr, Ti)B_2 nuclei, which exhibit an equiaxed polyhedral morphology. First-principles calculations on diborides [41] showed that the equilibrium morphology is mainly bounded by the {001} basal planes and two families of prismatic planes, {100} and {110}. Since both {100} and {110} are more stable than {001}, a rod-like grain morphology grown along the [001] direction is expected under equilibrium growth conditions. As the reaction proceeds, the B_2O_3 generated as a byproduct may preferentially passivate {110} [40], while the unpassivated {100} progressively grows out. Subsequently, the lateral growth was suppressed, and growth along the c axis became dominant, ultimately leading to the formation of rod-like (Hf,Zr,Ti)B_2 whiskers with a high aspect ratio.

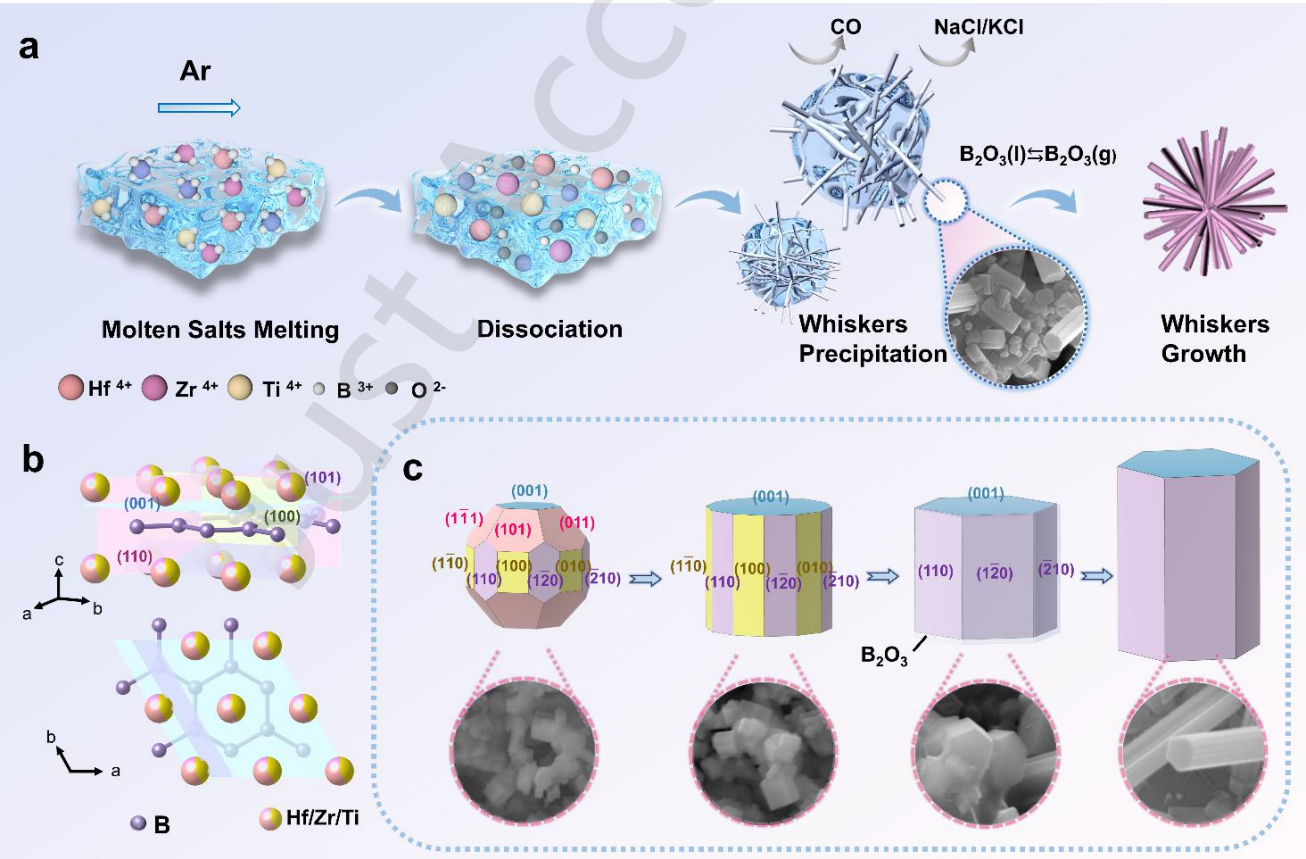


Fig. 5. Schematic diagram of the whisker growth mechanism: (a) macroscopic synthesis and growth process of the whiskers; (b) lattice structure of the (Hf,Zr,Ti)B_2; (c) microscopic morphological evolution and growth mechanism of the

Just Accepted

whiskers.

3.3 EMW absorption performance of whiskers

The electromagnetic response of the synthesized whisker samples was systematically characterized through the analysis of their complex permittivity ($\varepsilon_r = \varepsilon' - j\varepsilon''$) across the 2-18 GHz frequency range, where ε' represents the ability to polarize and store energy in an electric field, and ε'' denotes its capability to attenuate EMW energy. Based on the Debye relaxation theory, ε' and ε'' can be expressed by the following formulas [42]:

$$\varepsilon' = \varepsilon_\infty + \frac{\varepsilon_s - \varepsilon_\infty}{1 + \omega^2\tau^2} \quad \#(1)$$

$$\varepsilon'' = \frac{(\varepsilon_s - \varepsilon_\infty)}{1+\omega^2\tau^2}\omega\tau + \frac{\sigma}{\omega\varepsilon_0} \quad \#(2)$$

The relationship between the real part and imaginary part of the dielectric constant can be expressed as [43]:

$$\left(\varepsilon' - \frac{\varepsilon_s + \varepsilon_\infty}{2}\right)^2 + (\varepsilon'')^2 = \left(\frac{\varepsilon_s - \varepsilon_\infty}{2}\right)^2 \quad \#(3)$$

Herein, ε_∞ denotes the high-frequency limit of permittivity, ε_s represents the static permittivity, ω is the angular frequency of EMW, τ is the polarization relaxation time, σ stands for electrical conductivity, and ε_0 is the vacuum permittivity.

Fig. 6(a, b) shows the variation trends of the real part (ε') and imaginary part (ε''). It can be observed that both ε' and ε'' increase with increasing Ti content: the average ε' values rise from 9.98 (HZTB-1) to 12.28 (HZTB-3), while the average ε'' values increase from 2.21 to 7.84. This trend is primarily driven by the progressive intensification of lattice distortion as the Ti content increases. These distorted regions act as relaxation-type dipole centers that respond to alternating electromagnetic fields and dissipate energy through polarization relaxation, substantially increasing ε''. As the frequency increases, ε' exhibits a decreasing trend, which is known as the frequency

Just Accepted

dispersion (FD) effect, because the electronic and dipolar polarization fail to synchronize with the alternating field. The imaginary part ε" of HZTB-3 exhibits two distinct relaxation peaks, indicating the presence of multiple polarization relaxation processes. Additionally, the relaxation peaks in the ε" curves of HZTB-2 and HZTB-3 are broadened, which originates from the broader distribution of dipole polarization relaxation times induced by the greater lattice distortion and higher density of charge inhomogeneity sites with increasing Ti content.

The dielectric loss tangent (tanδ = ε"/ε') quantifies the electromagnetic energy dissipation capability relative to the total stored electromagnetic energy. As shown in Fig. 6(c), the average tanδ values of HZTB-1, HZTB-2, and HZTB-3 are 0.23, 0.42, and 0.83, respectively. Fig. 6(d) presents the Cole-Cole curves of the samples, in which each semicircle corresponds to a distinct Debye polarization relaxation process. Notably, the Cole-Cole curve of HZTB-1 exhibits a pronounced linear segment in its latter portion, which is the signature of conductive loss [44]. This feature is more conspicuous in HZTB-1 because, at lower Ti content, the overall polarization loss contribution is relatively limited; consequently, conductive loss constitutes a proportionally larger fraction of the total dielectric loss.

Moreover, microwave absorption performance is also governed by impedance matching characteristics (evaluated by Z) and the attenuation constant (α), which can be calculated using the following formulas [45,46]:

$$Z=\left|\frac{Z_{in}}{Z_0}\right|=\sqrt{\frac{\mu_r}{\varepsilon_r}}\tanh\left[j\left(\frac{2\pi fd}{c}\right)\sqrt{\mu_r\varepsilon_r}\right] \quad \#(4)$$

$$\alpha=\frac{2\pi f}{c}\sqrt{(\mu''\varepsilon''-\mu'\varepsilon')\sqrt{(\mu''\varepsilon''-\mu'\varepsilon')^2+(\mu''\varepsilon''+\mu'\varepsilon')^2}} \quad \#(5)$$

where f represents the EMW frequency, d is the sample thickness, c is the speed of light, Z_{in} is the input impedance, Z_0 is the free-space impedance, and μ_r and ε_r are the permeability and relative

Just Accepted

complex dielectric constant, respectively. Because the synthesized (Hf,Zr,Ti)B_2 whiskers are nonmagnetic, their relative complex permeability was taken as $\mu_r = 1$ ($\mu' = 1$, $\mu'' = 0$) in Eqs. (4) and (5). The α values in Fig. 6(e) indicate that HZTB-3 possesses the strongest electromagnetic attenuation capability among the three samples. However, the $|Z_{in}/Z_0|$ analysis at representative thicknesses of 2.25 mm, 2.35 mm, and 2.45 mm (Fig. 6(f-h)) reveals that the excessively high permittivity of HZTB-3 leads to impedance mismatch with free space. In contrast, HZTB-2 achieves superior impedance matching among the three samples.

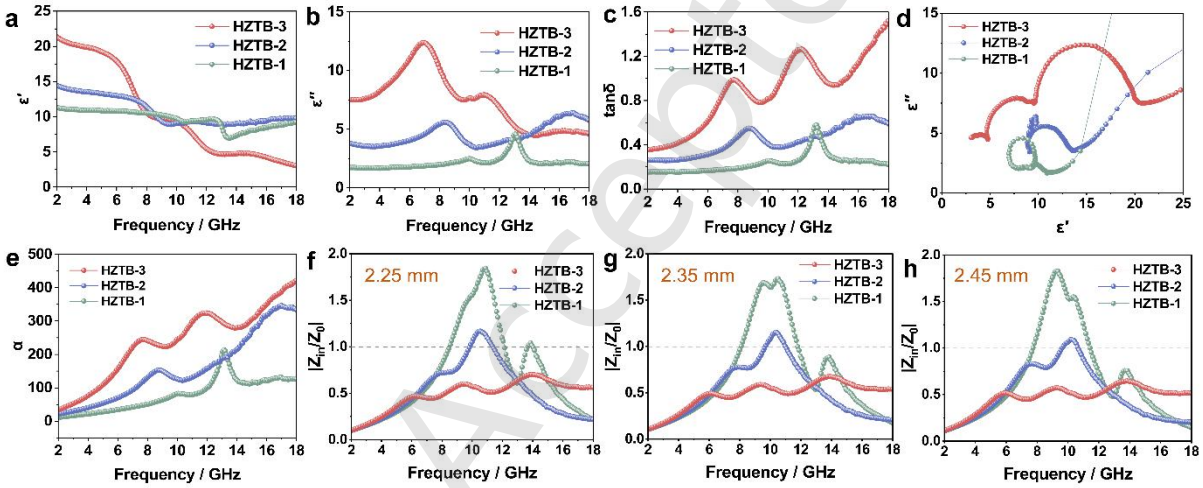


Fig. 6. Electromagnetic parameters of HZTB-1, HZTB-2, and HZTB-3 whiskers: (a) ε'; (b) ε''; (c) tanδ; (d) Cole-Cole curves; (e) α; (f-h) Impedance matching under different thicknesses.

According to the transmission line theory, the RL is evaluated by [47]:

$$RL = 20\lg\left|\frac{Z_{in}-Z_0}{Z_{in}+Z_0}\right| \quad \#(6)$$

The RL spectra of HZTB-1 to HZTB-3 are displayed in Fig. 7(a-f). HZTB-1 achieved a RL_{min} of -47.52 dB at 12.78 GHz with an EAB_{max} of 3.42 GHz. HZTB-2 yielded a RL_{min} of -60.88 dB at 9.99 GHz at a thickness of 2.55 mm. HZTB-3 showed a RL_{min} of only -17.58 dB and an EAB_{max} of 2.97 GHz. The superior room-temperature EMW absorption performance of HZTB-2 can be attributed to its balanced EMW attenuation capability and impedance matching. On the one hand, the moderate Ti content in HZTB-2 induces sufficient lattice distortion and dipole polarization loss while

Just Accepted

successfully avoiding the severe impedance mismatch. On the other hand, the three-dimensional interconnected network formed by the high-aspect-ratio whiskers enables electromagnetic waves to undergo multiple reflections, refractions, and scattering among the whiskers. Concurrently, the continuous whisker channels extend the propagation paths of the EMW and facilitate the long-range migration of electrons under the alternating electric field, thereby generating effective conduction loss. To verify the radar stealth potential, CST Studio was employed to simulate the RCS of a perfect electrical conductor (PEC) substrate coated with HZTB-1 and HZTB-2. Fig. 7(h-i) presents the corresponding three-dimensional radar scattering images, demonstrating significant RCS reductions and confirming the improved radar stealth performance of the whisker-structured ceramic composites.

Just Accepted

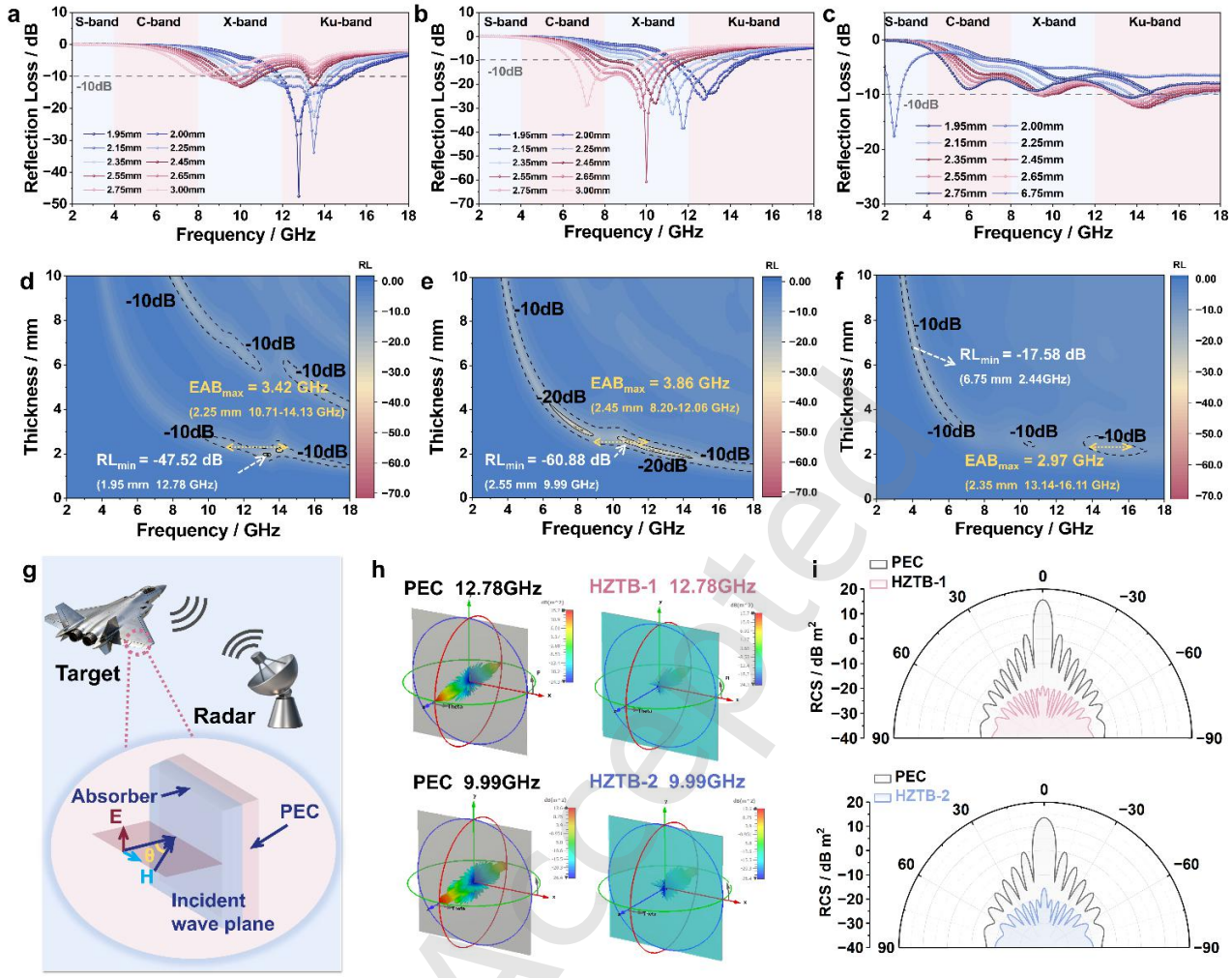


Fig. 7. EMW absorption performance of the samples: (a-c) RL curves at different thicknesses; (d-f) Two-dimensional RL contour maps; (g) Schematic diagram of RCS simulation; (h) Three-dimensional radar wave scattering signals of the PEC material and the substrates coated with HZTB-1 and HZTB-2; (i) Comparison of RCS attenuation values between HZTB-1 and HZTB-2 coatings.

To evaluate the structural stability and EMW absorption capability of the boride whiskers after exposure to an ultra-high-temperature environment, the as-prepared whisker powders were heat-treated at 1500 °C for 2 h. SEM and TEM observations (Fig. 8(a-f)) revealed that all samples maintained complete whisker morphology without structural collapse or coarsening, which verifies the high-temperature structural stability of the multi-component (Hf,Zr,Ti)B_2 system. TEM observations revealed that the surface oxide layers of the whiskers are significantly thinned compared to those at room temperature, particularly for HZTB-3, where the oxide layer thickness

Just Accepted

decreased from 5.72 nm to 2.39 nm. Notably, the lattice distortion induced by the cation radius mismatch in the (Hf,Zr,Ti)B_2 persists after heat treatment at 1500 °C, as confirmed by the bending and discontinuity of lattice fringes in the IFFT images (Fig. S7).

EMW absorption performance tests were conducted on the thermally treated whiskers, revealing that they still retained favorable EMW absorption performance. HZTB-1 attained an EAB_{max} of 5.04 GHz with an RL_{min} as low as -55.22 dB at 14.40 GHz, and HZTB-2 delivered an RL_{min} of -59.46 dB at 9.18 GHz at a thickness of 2.85 mm. Remarkably, HZTB-3, which exhibited relatively inferior performance at room temperature, achieved an RL_{min} of -55.08 dB at 14.04 GHz and an EAB_{max} of 8.64 GHz at a thickness of 2.50 mm, nearly covering the full X-band and the entire Ku-band. According to the TEM analysis in Fig. S6, HZTB-3 contains a fraction of particles encapsulated by an anomalously thick amorphous B_2O_3 layer. These insulating amorphous layers impede electron transport within the network, thereby reducing the EMW attenuation capability [39]. Consequently, despite HZTB-3 possessing a higher intrinsic dielectric loss, the limited electron transport resulted in insufficient impedance matching between the HZTB-3 surface and free space, causing most incident EMWs to be reflected rather than absorbed. In contrast, after heat treatment at 1500 °C, the substantial volatilization of B_2O_3 occurred [48], reducing the interfacial resistance at the whisker junctions and alleviating electron transport barriers within the conductive network. Therefore, EMWs can effectively penetrate into the HZTB-3 interior and are subsequently attenuated by the inherently strong loss capability. Aside from improving electron transport, the thinning of the B_2O_3 layer can strengthen the interfacial coupling between the conductive boride core and the thin oxide shell, thereby increasing both the interfacial adsorption energy and the interfacial dipole moment [39]. According to the Debye theory, the increase in the interfacial dipole moment is directly correlated

Just Accepted

with a prolonged polarization relaxation time (τ). The extended τ induces a more pronounced frequency-dependent decrease within the 2-18 GHz range, which is a hallmark of strong FD characteristics. This is reflected in Fig. 8(g), where the ε' curve of the heat-treated HZTB-3 exhibits a steeper frequency dependence compared to its pre-treated counterpart. This is further corroborated by the Cole-Cole curves (Fig. S8), which show a broadened relaxation-time distribution. According to the ideal permittivity framework for broadband EMW absorbers [39], achieving $|Z_{in}/Z_0| \approx 1$ across a full target frequency band at a single thickness requires ε′(f) to follow a specific negative-slope profile, as prescribed by an inverse-design criterion derived from transmission line impedance theory (Eq. S(10)). Physically, this arises because the quarter-wavelength matching thickness $d_m(f)$ becomes nearly frequency-independent when ε′(f) decreases steeply enough to offset the increase of f, thereby allowing a single fixed thickness to remain impedance-matched over a wider frequency window. Meanwhile, the ε″ values do not exhibit a significant decrease, suggesting that the associated lattice-distortion-induced polarization-loss capability is preserved. The tan δ curve of the heat-treated HZTB-3 (Fig. 8(i)) becomes flatter and broader across the 2-18 GHz range, which represents a characteristic dielectric feature for continuous and effective energy dissipation over a wide frequency band.

Just Accepted

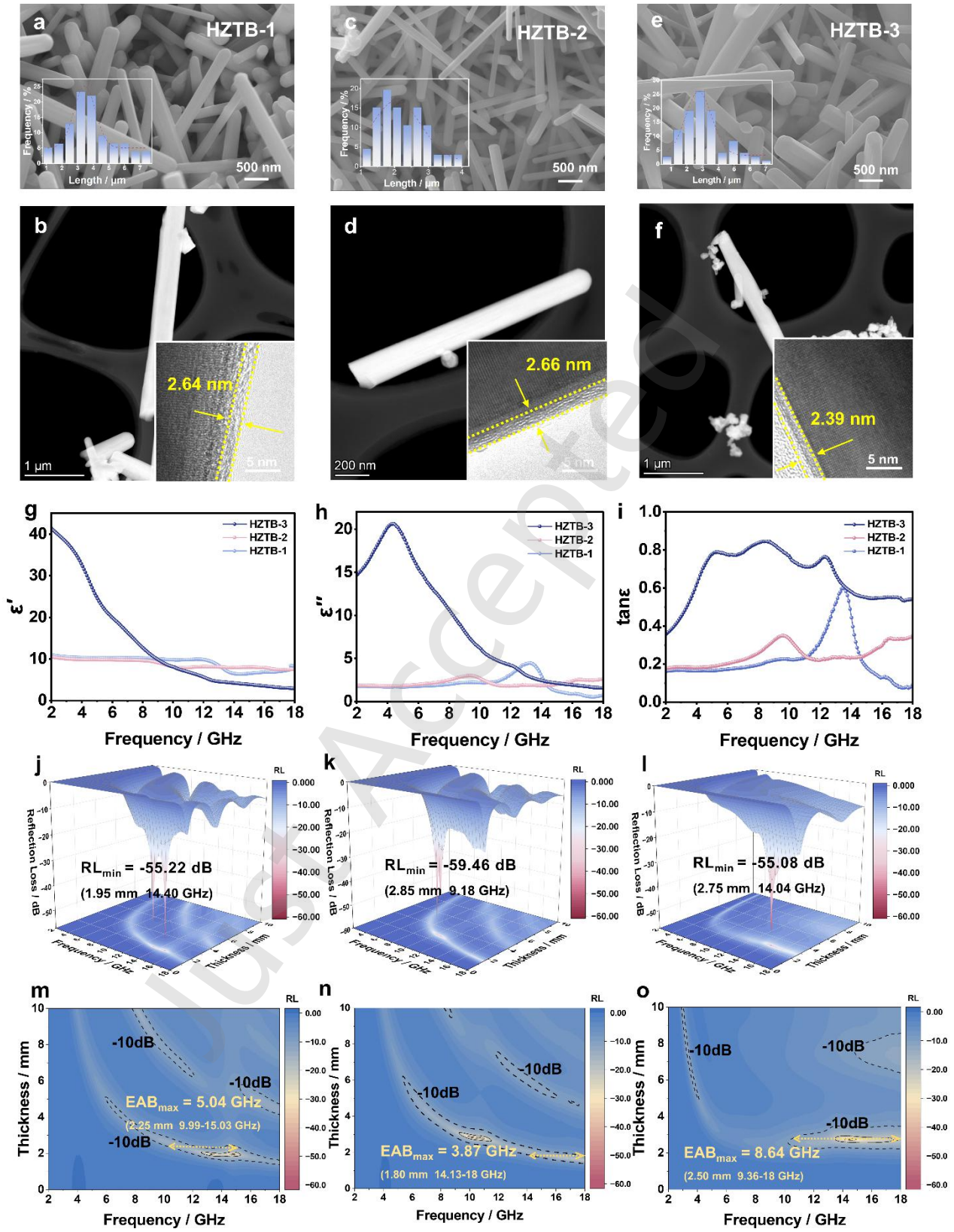


Fig. 8. SEM and HRTEM images and EMW absorption performance of HZTB-1 to HZTB-3 whiskers after heat treatment: (a, c, e) SEM images of HZTB-1 to HZTB-3; (b, d, f) TEM images of HZTB-1 to HZTB-3; (g–i) ε′, ε″, and tan δ of HZTB-1 to HZTB-3; (j-l) Three-dimensional RL maps; (m-o) Two-dimensional RL contour maps.

Just Accepted

In summary, the outstanding performance of the (Hf,Zr,Ti)B_2 whisker system originates from a dual-level synergistic effect (Fig. 9). At room temperature, the interconnected one-dimensional whisker geometry provides efficient electron transport pathways for conductive loss, while the multi-component solid solution composition introduces lattice-distortion-induced polarization centers for dielectric loss. The coordinated regulation of these two factors in HZTB-2 yields the optimal impedance matching and a remarkable RL_{min}. After high-temperature treatment, the substantial depletion of the thick insulating B_2O_3 layers eliminates electron transport barriers and generates a broad distribution of Maxwell–Wagner polarization relaxation times. These coupling effects result in enhanced impedance matching and stronger FD characteristics, which jointly extend the EAB_{max} of HZTB-3 from 2.97 GHz to 8.64 GHz. This value outperforms most of the reported diboride ceramic EMW absorbers, as demonstrated in the comparison chart in Fig. 9(b) [21–23,33,49–53].

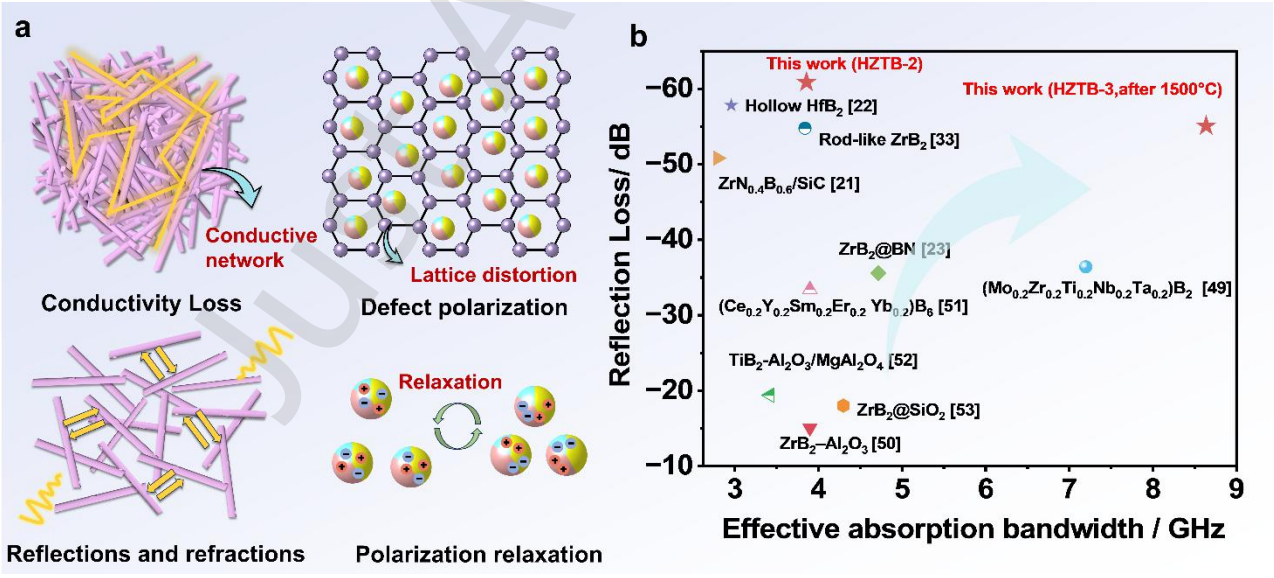


Fig. 9 (a) EMW absorption mechanism of (Hf,Zr,Ti)B_2 whiskers; (b) Comparison of the EMW absorption property of this work with other boride ceramic materials [21–23,33,49–53].

Just Accepted

4. Conclusion

In this work, an effective strategy to develop high-performance multi-component diboride whisker EMW absorbers via composition–structure synergy is successfully demonstrated. By constructing a high-aspect-ratio 1D whisker network and introducing lattice distortion via multi-principal cation modulation, the conductive loss pathways and polarization relaxation behaviors are efficiently regulated. Consequently, the HZTB-2 sample achieves a remarkable RL_{min} of -60.88 dB at a matching thickness of 2.55 mm. Crucially, the 1D whisker skeleton maintains exceptional structural integrity after heat treatment at 1500 °C, and the HZTB-3 sample exhibits an anomalous thermal-induced absorption leap, extending its maximum EAB to an ultra-wide 8.64 GHz at a thickness of 2.50 mm. This enhancement is fundamentally governed by thermal regulation-induced impedance-matching optimization and the intensification of dielectric FD characteristics. Additionally, RCS simulations confirm the practical and reliable radar stealth capability of the designed multi-component boride whiskers. This work establishes a fundamental design framework for the development of integrated structural, environmental, and electromagnetic protective systems operating in extreme environments.

Just Accepted

Acknowledgements

This work has been supported by the National Key R&D Program of China (Grant No. 2021YFA0715803), the National Natural Science Foundation of China (Grant Nos. 52293373 and 52402113), the Scientific and Technological Research Project of Henan Academy of Sciences (Grant No. 235200810094), the Startup Research Fund of Henan Academy of Sciences (Grant No. 241821029).

Declaration of interests

The authors declare no competing interests.

Electronic Supplementary Material: Supplementary Information is available in the online version of this article.

References

[1] Dai M, Jia Y, Deng Y, *et al.* An ultra‐broadband electromagnetic wave absorbing ZrB2-based ceramic composite inspired by barbule of peacock. *Small* 2024, **20**: 2405364.

[2] Dai G, Deng R, Zhang T, *et al.* Quantitative evaluation of loss capability for in situ conductive phase enhanced microwave absorption of high-Entropy transition metal oxides. *Adv. Funct. Mater.* 2022, **32**: 2205325.

[3] Ren B, Deng Y, Jia Y, *et al.* Electromagnetic wave absorbing ceramics composites made of polymer-derived SiC with BN@CNTs pyrolyzed higher than 1200 °C. *J. Mater. Sci. Technol.* 2023, **167**: 213–27.

[4] Wang W, Wang L, Huang J, *et al.* Multi-heterointerface lightweight ceramics achieving temperature-insensitive dielectric properties for high-temperature electromagnetic wave effective absorption. *J. Adv. Ceram.* 2025, **14**: 9221135.

[5] Ravinder D, Ravi Kumar G, Venudhar YC. Thermoelectric power studies of Ca–Co ferrites. *J. Alloys. Compd.* 2004, **368**: 38–43.

[6] Ma J, Huang Y, Huang H, *et al.* Fabrication of flexible flower-like ZIF-7-derived N-doped carbon composite films for high-efficiency electromagnetic wave absorption. *Carbon* 2026, **256**: 121644.

[7] Zhao J, Fu Y, Zhang Y, *et al.* Localized filtrating modification for fabricating gradient composites delivering lightweight and enhanced thermal protection. *J. Mater. Sci. Technol.* 2026, **245**: 152–63.

[8] Peng Z, Sun W, Xiong X, *et al.* Novel nitrogen-doped hafnium carbides for advanced ablation resistance up to 3273 K. *Corros. Sci.* 2021, **189**: 109623.

[9] Li J, Zhang Y, Zhao Y, *et al.* A novel $(Hf_{1/3}Zr_{1/3}Ti_{1/3})C$ medium-entropy carbide coating with

Just Accepted

excellent long-life ablation resistance applied above 2100 ◦C. *Composites, Part B* 2023, **251**: 110467.

[10] Zhang J, Fu Y, Lv J, *et al.* Tailoring ablation resistance of (Hf,Zr,Ta)C coatings above 2000 °C: Critical role of Ta content. *J. Adv. Ceram.* 2026, **15**: 9221207.

[11] Li W, Lv J, Shi X, *et al.* A functionally graded C/C-HfC-SiC composite sharp leading edge merging lightweight and superior ablation resistance. *Composites, Part B* 2025, **306**: 112783.

[12] Du B, Liu H, Chu Y. Fabrication and characterization of polymer-derived high-entropy carbide ceramic powders. *J. Am. Ceram. Soc.* 2020, **103**: 4063–8.

[13] Lv J, Li W, Li T, *et al.* Multicomponent (Hf-Zr-Ta)B_2 coatings for carbon/carbon composites and structural optimization enabling superior ablation resistance. *J. Mater. Sci. Technol.* 2025, **204**: 115–26.

[14] Gild J, Zhang Y, Harrington T, *et al.* High-Entropy Metal Diborides: A New Class of High-Entropy Materials and a New Type of Ultrahigh Temperature Ceramics. *Sci. Rep.* 2016, **6**: 37946.

[15] Cheng Y, Hu P, Dong S, *et al.* Dual bionics of structure and preparation: Gradient architectured carbon/ ceramic composite as light as water but bearing ultra-high temperature max to 2500 ◦C. *Composites, Part B* 2023, **265**: 110963.

[16] Li X, Zhang Y, Fu Y, *et al.* From molecular precursors to ultra-high temperature ceramics: A novel synthesis of hafnium carbonitride nanoceramics. *J. Mater. Sci. Technol.* 2025, **223**: 11–21.

[17] Monteverde F, Bellosi A. Efficacy of HfN as sintering aid in the manufacture of ultrahigh-temperature metal diborides-matrix ceramics. *J. Mater. Res.* 2004, **19**: 3576–85.

[18] Ni D, Cheng Y, Zhang J, *et al.* Advances in ultra-high temperature ceramics, composites, and coatings. *J. Adv. Ceram.* 2022, **11**: 1–56.

[19] Wang Q, Qi L, Jia Y, *et al.* Flexible ZrO_2/ZrC/ZrB_2 ceramic nanofiber mats by electrospinning with broadband electromagnetic absorption and high-temperature oxidation resistance. *Mater. Lett.* 2024, **365**: 136442.

[20] Deng Y, Ren B, Jia Y, *et al.* Layered composites made of polymer derived SiOC/ZrB_2 reinforced by ZrO_2/SiO_2 fibers with simultaneous microwave absorption and thermal insulation. *J. Mater. Sci. Technol.* 2024, **196**: 50–9.

[21] Jian X, Tian W, Li J, *et al.* High-Temperature oxidation-resistant $ZrN_{0.4}$ $B_{0.6}$/ SiC nanohybrid for

Just Accepted

enhanced microwave absorption. *ACS Appl. Mater. Interfaces* 2019, **11**: 15869–80.

[22] Zhang H, Wang T, Shen C, *et al.* Synthesis of hollow-spherical-structured HfB_2 with superior electromagnetic wave absorption performance. *J. Alloys. Compd.* 2025, **1049**: 185358.

[23] Yang L, Chen T, Liu Y, *et al.* Synergistic multiple microwave attenuation of ZrB_2@BN composites as thin and efficient microwave absorbing materials. *Ceram. Int.* 2025, **51**: 32251–66.

[24] Lv J, Li W, Li T, *et al.* Ablation behavior of high-entropy boride (Hf-Zr-Ta-Ti)B_2 coating fabricated via supersonic atmospheric plasma spraying for carbon/carbon composites. *Composites, Part B* 2024, **270**: 111137.

[25] Liu J, Liu D, Gu J, *et al.* Six-principal-component high-entropy IVB–VB diborides: Low-temperature synthesis, microwave absorption, and mechanisms. *J. Am. Ceram. Soc.* 2025, **108**: e20350.

[26] Feng L, Fahrenholtz WG, Brenner DW. High-entropy ultra-high-temperature borides and carbides: a new class of materials for extreme environments. *Annu. Rev. Mater. Res.* 2021, **51**: 165–85.

[27] Li J, Lu F, Fu Y, *et al.* The oxidation/ablation differences of multi-phase carbide ceramics evaluated by atomic simulations and performance data validation. *Composites, Part B* 2025, **302**: 112552.

[28] Jia Z, Guo Z, Ma H, *et al.* Polymetallic cation doping induced vacancy engineering for synergistically enhanced electromagnetic wave absorption. *Carbon* 2026, **251**: 121357.

[29] Yuan M, Weible AH, Azadi F, *et al.* Advancements in high-entropy materials for electromagnetic wave absorption. *Mater. Horiz.* 2025, **12**: 1033–57.

[30] Zhu Y, Guan L, Duan C, *et al.* High-entropy transition metal carbide nanowires with enhanced microwave absorption properties. *J. Mater. Sci. Technol*. 2025, **224**: 302–11.

[31] Zhang W, Dai FZ, Xiang H, *et al.* Enabling highly efficient and broadband electromagnetic wave absorption by tuning impedance match in high-entropy transition metal diborides (HE TMB_2). *J. Adv. Ceram.* 2021, **10**: 1299–316.

[32] Hu P, Xu J, Dong S, *et al.* Compositional and structural engineering of multicomponent borides hollow microspheres with superior microwave absorption performance. *J. Mater. Sci. Technol.* 2026, **247**: 81–94.

Just Accepted

[33] Liu S, Dai M, Jia Y, *et al.* Electromagnetic wave-absorbing of polymer derived rod-like ZrB_2 ultrahigh-temperature ceramic composites. *J. Eur. Ceram. Soc.* 2024, **44**: 7668–79.

[34] Greczynski G, Hultman L. A step-by-step guide to perform x-ray photoelectron spectroscopy. *J. Appl. Phys.* 2022, **132**: 011101.

[35] Li X, Tang J, Qiao J, *et al.* Oxidation mechanism and kinetics of TiB_2 submicron powders in air. *J. Am. Ceram. Soc.* 2025, **108**: e20135.

[36] Qiu XL, Gao XH, He CY, *et al.* Structure, optical simulation and thermal stability of the HfB_2-based high-temperature solar selective absorbing coatings. *RSC Adv.* 2019, **9**: 29726–33.

[37] Armitage R, Suda J, Kimoto T. Characterization of ZrB_2 (0 0 0 1) surface prepared by ex situ HF solution treatment toward applications as a substrate for GaN growth. *Surf. Sci.* 2006, **600**: 1439–49.

[38] Liu D, Liu H, Ning S, *et al.* Chrysanthemum-like high-entropy diboride nanoflowers: A new class of high-entropy nanomaterials. *J. Adv. Ceram.* 2020, **9**: 339–48.

[39] Ren B, Jia Y, Qi L, *et al.* Broadband electromagnetic absorption up to 1473 K enabled by dielectric frequency-dispersion engineering in ceramic composites. *Nat. Commun.* 2025, **17**: 318.

[40] Chen Z, Zhao X, Li M, *et al.* Synthesis of rod-like ZrB_2 crystals by boro/carbothermal reduction. *Ceram. Int.* 2019, **45**: 13726–31.

[41] Sun W, Liu J, Xiang H, *et al.* A theoretical investigation on the anisotropic surface stability and oxygen adsorption behavior of ZrB_2. *J. Am. Ceram. Soc.* 2016, **99**: 4113–20.

[42] Fu Y, Huang Y, Huang Q, *et al.* Gradient pyrolysis-derived multiphase heterogeneous interfaces for enhanced electromagnetic wave absorption. *Carbon* 2026, **247**: 121013.

[43] Guan H, Wang Q, Wu X, *et al.* Biomass derived porous carbon (BPC) and their composites as lightweight and efficient microwave absorption materials. *Composites, Part B* 2021, **207**: 108562.

[44] Liu C, Feng X, Liu S, *et al.* Graphene reinforced nanoarchitectonics of 3D interconnected magnetic-dielectric frameworks for high-efficient and anti-corrosive microwave absorbers. *J. Mater. Sci. Technol.* 2024, **168**: 194–207.

[45] Liu H, Liu B, Deng J, *et al.* Electrically conductive yet thermally insulating SiC nanowire aerogels enabled by vertical graphene nanosheet arrays. *Carbon* 2026, **252**: 121399.

Just Accepted

[46] Jia Y, Wu X, Ren B, *et al.* Electromagnetic wave absorption of polymer derived ceramic composites tuned by multi-component oxide solid solution. *Composites, Part B* 2024, **278**: 111431.

[47] Du X, Liu Y, Su X, *et al.* Dramatic integrated enhancement of electromagnetic wave absorption and delamination resistance via 3D interlayer network architecture in composites. *Carbon* 2026, **246**: 120872.

[48] Wen Z, Meng H, Jiang S, *et al.* Non-equimolar (Hf,Zr,Ta,W)B_2 high-entropy diborides enable superior oxidation resistance. *Sci. China. Mater.* 2023, **66**: 3213–22.

[49] Liu C, Chen Q, Li X, *et al.* Low-temperature synthesis of a novel diboride ceramic with electromagnetic wave absorption properties. *J. Mater. Sci.: Mater. Electron.* 2024, **35**: 287.

[50] Zhang W, Zhang Z, Zhao F, *et al.* High-temperature stability of wave absorption properties for SiC enhanced ZrB_2–Al_2O_3 ceramics. *Ceram. Int.* 2024, **50**: 33571–80.

[51] Zhang W, Zhao B, Xiang H, *et al.* One-step synthesis and electromagnetic absorption properties of high entropy rare earth hexaborides (HE REB_6) and high entropy rare earth hexaborides/borates (HE REB_6/HE $REBO_3$) composite powders. *J. Adv. Ceram.* 2021, **10**: 62–77.

[52] Liu X, Zhang S, Luo H, *et al.* Temperature-insensitive microwave absorption of TiB_2-Al_2O_3/$MgAl_2O_4$ ceramics based on controllable electrical conductivity. *Sci. China. Technol. Sci.* 2021, **64**: 1250–63.

[53] Ma X, Logesh K, Mohammed J, *et al.* Enhancement of microwave absorption properties of bilayer absorber comprising of ZrB_2@SiO_2 composite and poly-ortho toluidine (PoTo) in 2–18 GHz frequency. *Ceram. Int.* 2023, **49**: 4505–16.

Just Accepted

Electronic Supplementary Material

Multi-component ultra-high-temperature boride ceramic whiskers with enhanced electromagnetic wave absorption

Yixin Li[1], Yanqin Fu[2]*, Junhao Zhao[1], Jian Zhang[1], Qingzhe Cui[1], Jiachen Li[1], Junshuai Lv[1], Liyuan Han[2], Ruiyi Su[3], Tien Zhang[3], Yulei Zhang[1,2]*, and Hejun Li[1]

[1] *Shaanxi Key Laboratory of Fiber Reinforced Light Composite Materials, Science and Technology on Thermostructural Composite Materials Laboratory, Northwestern Polytechnical University, Xi'an, 710072, China*

[2] *Henan Key Laboratory of High Performance Carbon Fiber Reinforced Composites, Institute of Carbon Matrix Composites, Henan Academy of Sciences, Zhengzhou 450046, China*

[3] *General Design Department of Beijing Mechanical and Electrical Engineering, Beijing 100089, China*

**Corresponding author.*

✉Address correspondence to Yanqin Fu, fuyanqin@hnas.ac.cn; Yulei Zhang, zhangyulei@nwpu.edu.cn

Supporting information to https://doi.org/10.26599/NR.2026.94909271

Just Accepted

Part 1. Thermodynamic analysis was employed to determine the feasibility of preparation via the thermal reduction method

Taking HZTB-1 as an example, in this reaction, HfO_2, ZrO_2, TiO_2, and B_4C serve as the reaction raw materials, while NaCl/KCl acts as the molten salt medium without participating in the reaction. Therefore, the possible reactions and the correlation between the standard Gibbs free energy($\Delta G^{\theta}_{R,T}$) of these reactions and temperature (℃) are as follows [1,2] :

$$HfO_2+\frac{5}{7B_4C}=HfB_2+\frac{3}{7B_2O_3(l)}+\frac{5}{7CO(g)}\#(1)$$

$$\Delta G^{\theta}_{R,T}=210.987-0.135T$$

$$ZrO_2+\frac{5}{7B_4C}=ZrB_2+\frac{3}{7B_2O_3(l)}+\frac{5}{7CO(g)}\#(2)$$

$$\Delta G^{\theta}_{R,T}=199.790-0.134T$$

$$TiO_2+\frac{5}{7B_4C}=TiB_2+\frac{3}{7B_2O_3(l)}+\frac{5}{7CO(g)}\#(3)$$

$$\Delta G^{\theta}_{R,T}=91.139-0.13T$$

$$\frac{9}{20HfB_2}+\frac{9}{20ZrB_2}+\frac{1}{10TiB_2}=(Hf_{0.45}Zr_{0.45}Ti_{0.1})B_2\#(4)$$

$$\Delta G^{\theta}_{R,T}=\Delta G^{M}_{R,T}$$

$$\frac{9}{20HfO_2}+\frac{9}{20ZrO_2}+\frac{1}{10TiO_2}+\frac{5}{7B_4C}=(Hf_{0.45}Zr_{0.45}Ti_{0.1})B_2+\frac{3}{7B_2O_3}+\frac{5}{7CO}\#(5)$$

$$\Delta G^{\theta}_{R,T}=193.964-0.134T+\Delta G^{M}_{R,T}$$

Among them, $\Delta G^{\theta}_{R,T}$ represents the molar Gibbs free energy of mixing of HZTB-1. Due to the similar interatomic interactions, under ideal conditions, it satisfies:

$$\Delta G^{M}_{R,T}=-T\Delta S_{mix}\#(6)$$

Just Accepted

Among them, ΔS_{mix} represents the molar entropy of mixing of HZTB-1, which is defined as:

$$\Delta S_{mix}=-\frac{R}{3}\sum_{i=1}^{N} x_i \ln x_i \quad \#(7)$$

In the equation, R represents the ideal gas constant (J/mol·K), N denotes the number of element types in the metal sublattice of the ternary solid solution, and Xi is the molar fraction of the i-th element in the sublattice. Based on the reaction, the ΔS_{mix} of HZTB-1 is calculated to be 0.32R. Therefore, the Gibbs free energies of Reactions (4) and (5) are -0.0026T and 193.964 - 0.137T, respectively.

Part 2. Prediction of solid solution formation ability

$$\delta_a=\sqrt{\sum_{i=1}^{N} X_i\left[1-a_i/\left(\sum_{i=1}^{N} X_i a_i\right)\right]^2} \quad \#(8)$$

$$\delta_c=\sqrt{\sum_{i=1}^{N} X_i\left[1-c_i/\left(\sum_{i=1}^{N} X_i c_i\right)\right]^2} \quad \#(9)$$

In the formula:

N —— Number of components of the multi-component solid solution;

a_i and c_i —— Lattice constants of the i-th MB_2 ;

X_i —— Molar content of the i-th component.

After calculation, the δ_a and δ_c of HZTB-1 are 1.2% and 2.6%, respectively; the δ_a and δ_c of HZTB-2 are 1.6% and 3.4%, respectively; the δ_a and δ_c of HZTB-3 are 1.9% and 4.1%, respectively. Therefore, the δ criterion indicates that the preparation of the above three types of boride ceramics is theoretically feasible. Among them, HZTB-1 has the smallest δ, suggesting that it is the easiest to synthesize a

Just Accepted

single-phase solid solution in this case.

Part 3. Quarter- wavelength interference- cancellation model for broadband impedance matching

The connection between a steep FD in ε′ and a broadened impedance-matching window arises from the quarter-wavelength interference-cancellation model [3,4]:

$$d_m(f)=\frac{nc}{4f\sqrt{|\varepsilon_r(f)|}}\ (n=1, 3, 5\ldots)\#(10)$$

In the formula:

$d_m(f)$ —— Frequency-dependent matching thickness;

n —— Order of quarter-wavelength interference;

c —— Speed of light in vacuum;

$|\varepsilon_r(f)|$ —— Modulus of the complex permittivity.

For a non-magnetic absorber, the matching thickness that satisfies $|Z_{in}/Z_0| \approx 1$ scales as $d_m(f)$. When ε′ is frequency-independent, $d_m(f)$ varies approximately as 1/f, so a fixed physical thickness only satisfies the matching condition within a narrow frequency window. However, when ε′(f) decreases steeply with frequency, this decrease compensates for the increase of f in the denominator, keeping $d_m(f)$ nearly constant over a wide frequency range, thereby allowing a single fixed thickness to remain impedance-matched across a much broader band

Just Accepted

Part 4. Figures and tables

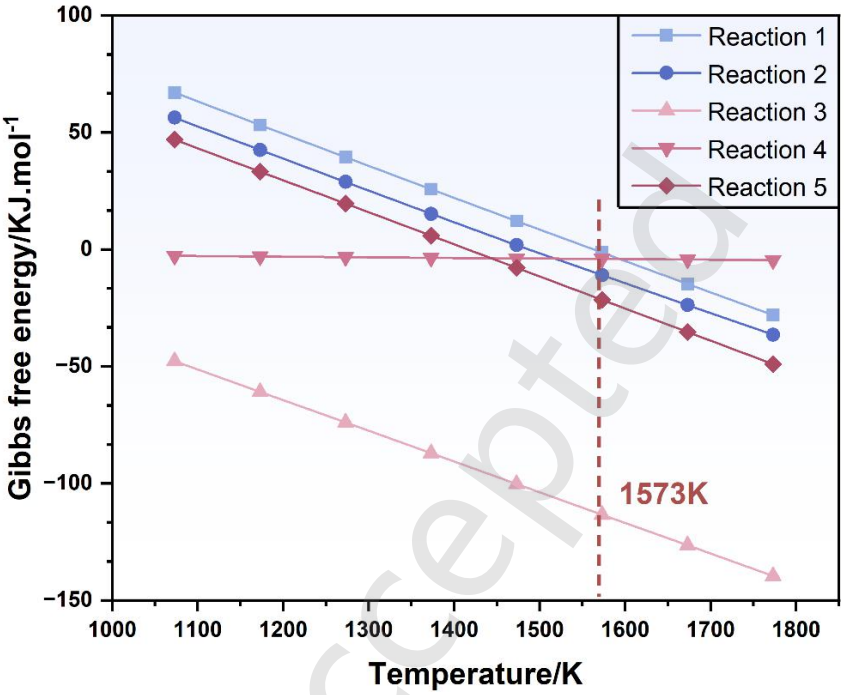


Fig. S1. Variation of standard Gibbs free energy of Reactions (1) to (5) with temperature (K).

Just Accepted

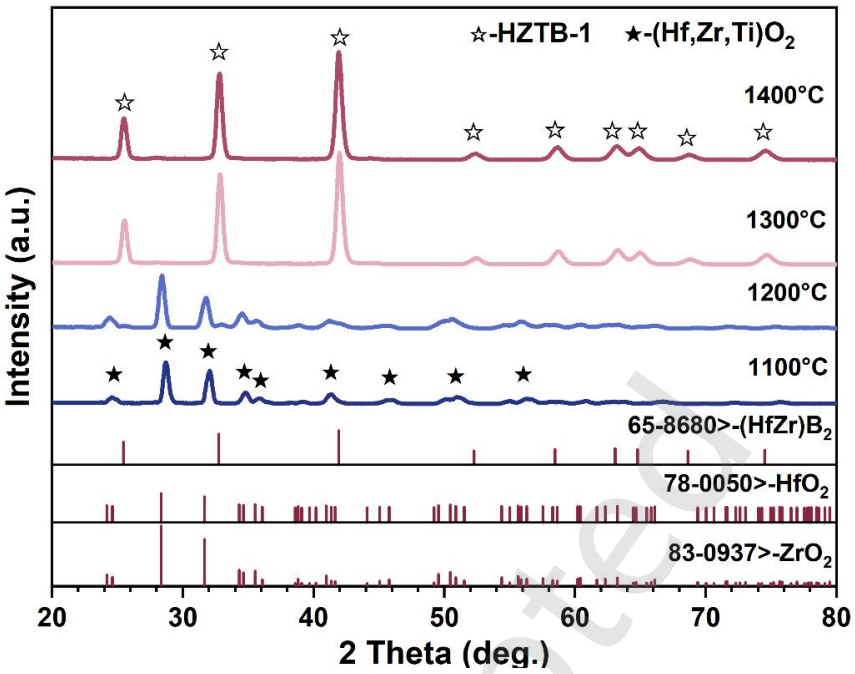


Fig. S2. XRD patterns of HZTB-1 prepared at different temperatures.

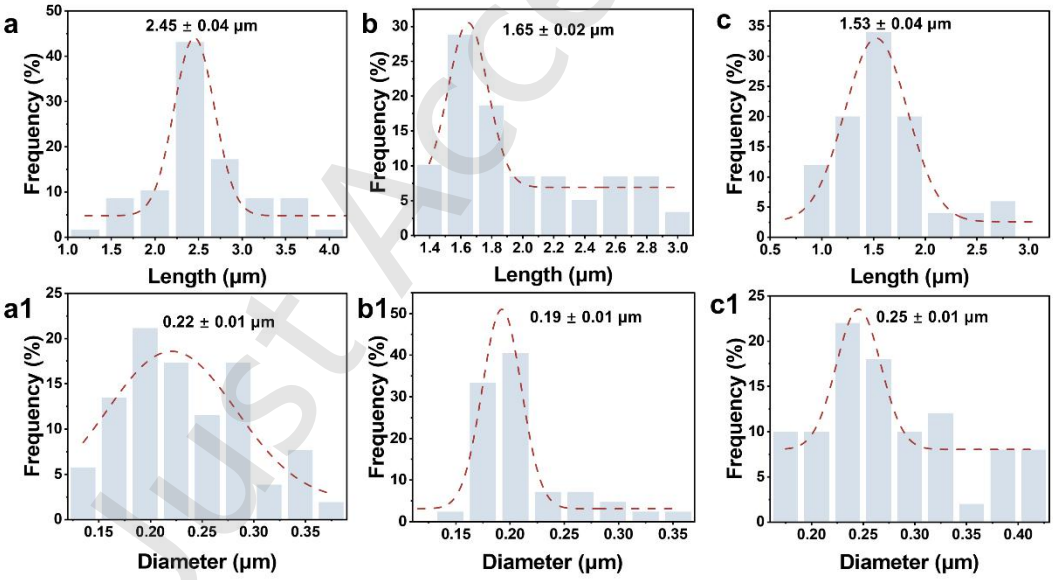


Fig. S3. Length and diameter distribution histograms of (a-a1) HZTB-1; (b-b1) HZTB-2; (c-c1) HZTB-3.

Just Accepted

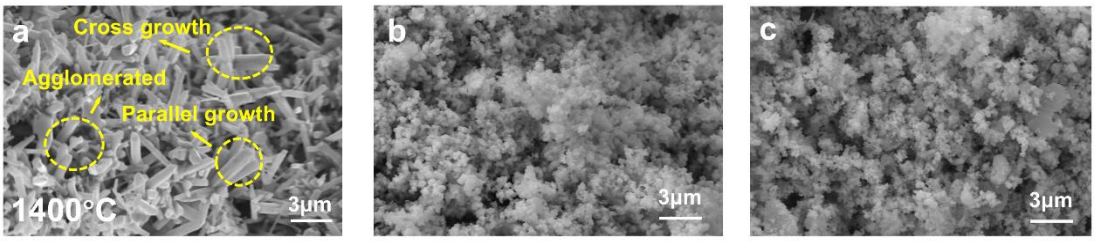


Fig. S4. SEM images of products with different element ratios prepared at 1400 °C: (a)HZTB-1; (b) HZTB-2; (c) HZTB-3.

Table S1. Unit Cell Parameters and Bond Lengths of HfB_2, ZrB_2, TiB_2, and HZTB-1 Obtained from XRD Pattern Refinement.

Materials	a(Å)	c(Å)	B-B(Å)	M-B(Å)
HfB_2	3.141	3.470	1.813	2.510
ZrB_2	3.169	3.530	1.830	2.540
TiB_2	3.028	3.228	1.745	2.357
HZTB-1	3.154	3.499	1.821	2.526

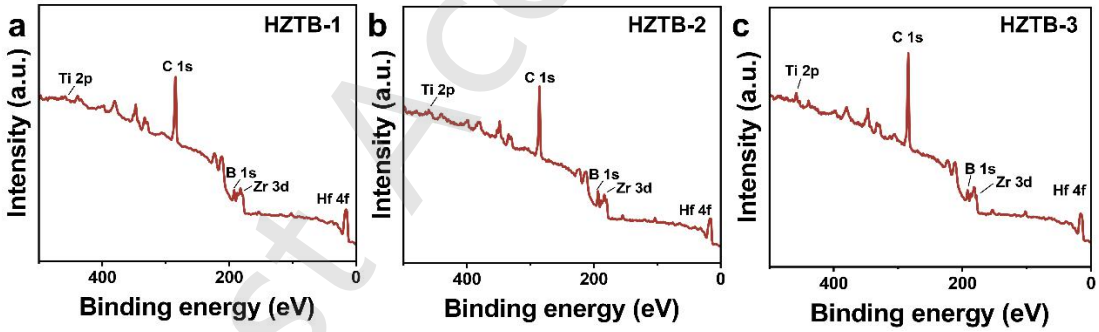


Fig. S5. XPS survey spectrum of (a) HZTB-1; (b) HZTB-2; (c) HZTB-3.

Just Accepted

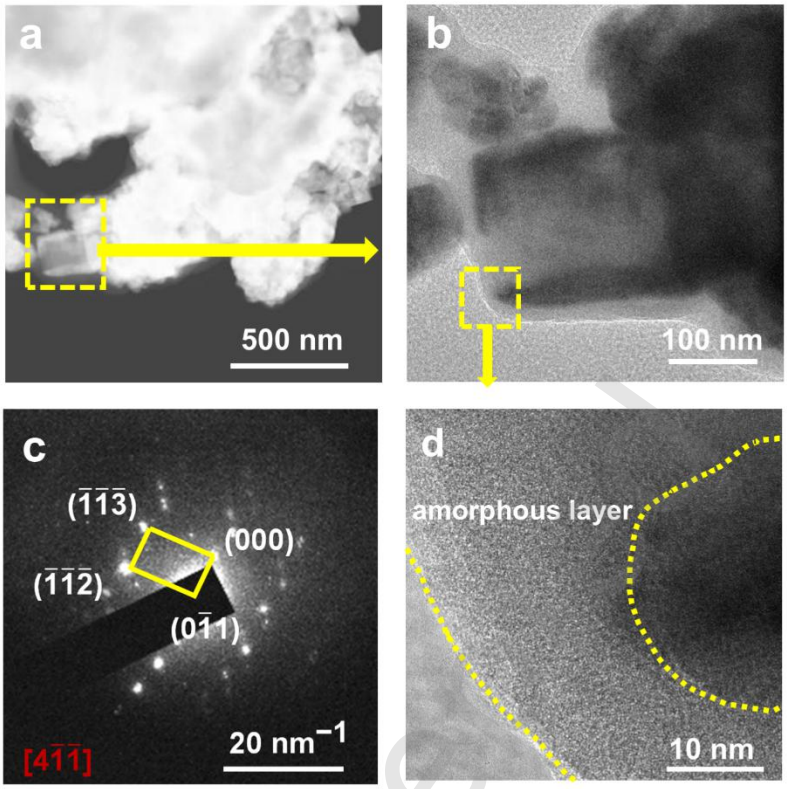
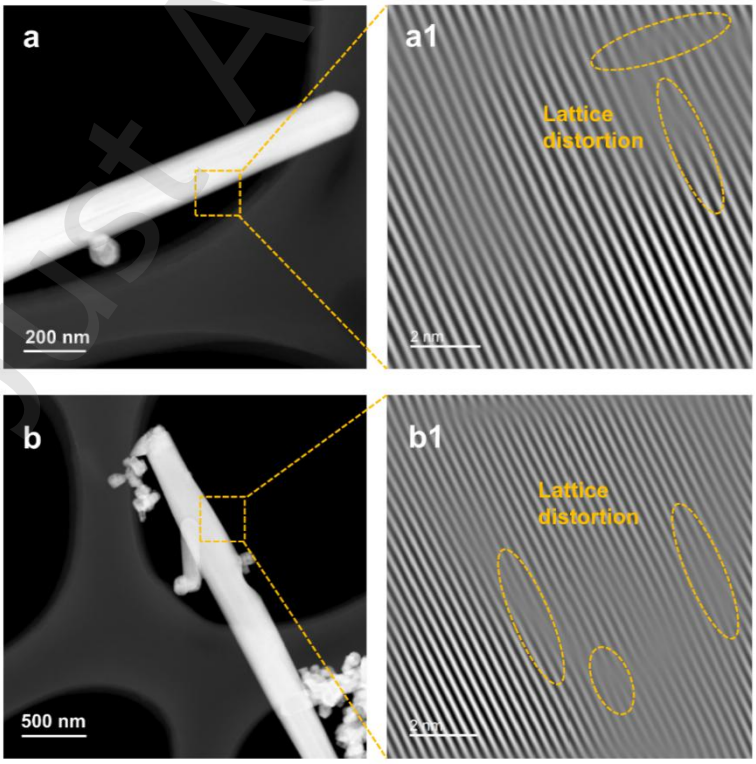


Fig. S6. (a)-(b) TEM images of HZTB-3; (c) SAED pattern; (d) HRTEM image of the yellow-marked region in (b).



Just Accepted

Fig. S7. TEM and IFFT images of HZTB-2 and HZTB-3 after heat treatment.

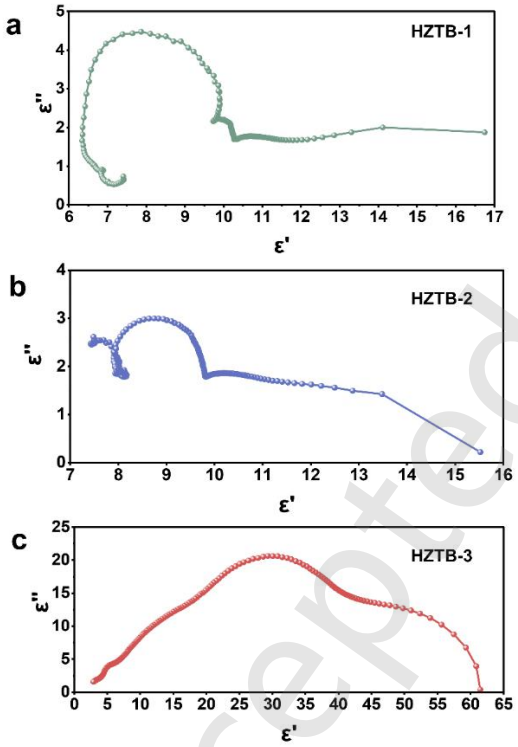


Fig. S8. Cole–Cole curves of HZTB-1, HZTB-2, and HZTB-3 whiskers after heat treatment.

Reference

[1] Liu D, Wen T, Ye B, et al. Synthesis of superfine high-entropy metal diboride powders. *Scr. Mater*. 2019, 167: 110–4.

[2] Wen T, Ning S, Liu D, et al. Synthesis and characterization of the ternary metal diboride solid‐solution nanopowders. *J. Am. Ceram. Soc.* 2019, 102: 4956–62.

[3] Zhang K, Liu Y, Li X, et al. All‐Dielectric Ultra‐Broadband Microwave Absorbing Aerogel with Optimized Dielectric Dispersion via Dielectric Relaxation Time Regulation. *Adv. Mater.* 2025, 37: 2506386.

[4] Lv H, Yang Z, Pan H, et al. Electromagnetic absorption materials: Current progress and new frontiers. *Prog. Mater. Sci*. 2022, 127: 100946.

Just Accepted